PAPER

Growth and branching of gold nanoparticles through mesoporous silica thin films†

Paula C. Angelomé,*[a] Isabel Pastoriza-Santos,[a] Jorge Pérez-Juste,[a] Benito Rodríguez-González,[a] Andrés Zelcer,[bc] Galo J. A. A. Soler-Illia[bd] and Luis M. Liz-Marzán*[a]

Composite materials made of mesoporous oxide thin films containing metallic nanoparticles are of high interest in various fields, including catalysis, biosensing and non-linear optics. We demonstrate in this work the fabrication of such composite materials containing a sub-monolayer of gold nanoparticles (GNPs) of various shapes covered with mesoporous silica thin films. Additionally, the shape of the GNPs (and thus their optical properties) can be modified *in situ* through seeded growth and branching. Such growth proceeds upon wetting with $HAuCl_4$ solution, a surfactant (cetyltrimethylammonium bromide, CTAB) and a mild reducing agent (ascorbic acid, AA). The effect of varying several reaction parameters (time and CTAB and AA concentrations) was evaluated, showing that more anisotropic particles are obtained at longer reaction times, lower CTAB concentration and higher AA concentration. The final shape of the GNPs was also found to depend on their initial shape and size, as well as the pore size of the mesoporous film covering them. Because the growth proceeds through the pores of the film, it may lead to shapes that are not easily obtained in solution, such as particles with branches on one side only. Finally, we have confirmed that no damage was induced to the mesoporous silica structure during the growth process and thus the final particles remain well covered by the thin film, which can eventually be used as a filter between the GNPs and the outer medium.

Introduction

Gold nanoparticles (GNPs) have acquired an enormous interest in the scientific community due to their interesting properties and their potential applications in fields as diverse as catalysis, plasmonics, metamaterials, ultrasensitive sensing and cancer therapy.[1,2] Much of this interest has been driven by their fascinating optical properties, related to localized surface plasmon resonances (LSPRs),[3,4] which give rise to intense extinction bands in the visible and NIR, as well as high electric field enhancements at the nanoparticle surface.[5] The optical response of GNPs can be tuned by changes in their size and shape, as well as their dielectric environment (refractive index of the surrounding medium, presence of neighboring particles, *etc.*).[6]

Thus, controlling the synthesis methods to produce GNPs, the optical properties can be tuned according to specific applications. Due to this close relationship between synthesis, optical properties and possible applications, the synthesis of GNPs has been extensively developed during the past decades[7] and a wide variety of morphologies can be obtained in a reproducible way by means of colloid chemistry methods. Readily obtainable morphologies include spheres, rods, various polyhedra, stars and plates.[7,8] GNPs presenting sharp tips and edges are particularly interesting, as it has been demonstrated that such features provide them with a high sensitivity toward local changes in their dielectric environment and the ability to generate large electric field enhancements close to their surface,[9] making this type of particles ideal for surface enhanced Raman scattering (SERS) and LSPR based (bio)sensors.

Having recognized the interest and importance of metal nanoparticles, their incorporation within functional materials may result in composites with added value. For example, if GNPs are covered with a porous film, at least two additional features are added to the final material: the capability of filtering and selecting which moieties may ultimately reach the particles and the enhanced stability of the metal nanoparticle component. In the field of porous materials, the synthesis of ordered mesoporous materials has experienced an outstanding development during the last fifteen years.[10–12] These materials are obtained by

[a]Departamento de Química Física-Universidade de Vigo, 36310, Vigo, Spain. E-mail: angelome@uvigo.es; lmarzan@uvigo.es
[b]Gerencia Química, Centro Atómico Constituyentes, Comisión Nacional de Energía Atómica, Av. Gral Paz 1499, B1650KNA, San Martín, Buenos Aires, Argentina
[c]Escuela de Ciencia y Technología-Universidad de San Martín, Buenos Aires, Argentina
[d]Departamento de Química Inorgánica, Analítica y Química Física, Facultad de Ciencias Exastas y Naturales, Universidad de Buenos Aires, Buenos Aires, Argentina
† Electronic supplementary information (ESI) available. See DOI: 10.1039/c2nr11547f

combination of two processes: sol–gel reactions and self-assembly of amphiphilic molecules that act as templates, resulting in the formation of materials with highly ordered arrays of monodisperse pores and high specific surface areas.

Numerous examples have been reported regarding the combination of mesoporous oxide thin films with metallic nanoparticles,[13–18] mainly aimed at applications in catalysis, biosensing and non-linear optics. Such composites are typically obtained by two alternative methods: (a) embedding preformed nanoparticles during the synthesis of the sol–gel material and (b) in situ synthesis of the nanoparticles inside the preformed porous oxide, typically by impregnation with the metal salt and subsequent reduction. In method a, the shape and composition of the particles are restricted to those that are stable during sol preparation (usually highly acidic medium) and oxide formation (often including a high temperature step), while the presence of particles and their capping agents can also alter the formation of the pores and the stability of the sol. On the other hand, in method b the modulation of the size and shape of the particles is limited by the size and shape of the pores, whereas the control of nucleation and growth processes is a critical issue, as nanoparticles easily nucleate at the film surface rather than in the interior of the pores. It has additionally been demonstrated that the mesoporous 3D structure as well as pore size can affect the mass transport through the pores[19–21] and thus the photocatalytic activity of the composite material.[22] However, this aspect has been seldom applied to control the growth of nanoparticles or other materials embedded inside the pores.[23,24]

We present here the preparation of composite materials comprising a sub-monolayer of GNPs covered with a sol–gel mesoporous silica thin film and the subsequent modification of the particles shape by chemical growth, taking advantage of the mesoporous structure. The first step of the synthesis[25] allows obtaining fully covered GNPs of arbitrary shapes (spheres, decahedra, and stars) and well-ordered mesoporous thin films. Because the particles are synthesized prior to thin film formation, their initial shape and size can be finely tuned by means of well-known colloid chemistry methods. Additionally, the particles are perfectly localized at the substrate–film interface, as they are initially adsorbed onto the substrate by strong interactions that are not affected by thin film preparation. In a second step, the GNP shape was modified by seeded growth, under various experimental conditions. We found clear evidence that the mesoporous material has a strong influence on the particle growth process, ultimately allowing the production of novel GNP shapes that are neither easily obtained in solution nor easily encapsulated within oxide films. Among the various composite materials obtained, the most interesting ones are probably those containing "hairy" GNPs encapsulated within porous films, since they can find applications through a combination of the field enhancement properties of the metallic tips with the filtering ability of the mesoporous material.

Experimental

Materials

HAuCl$_4$·3H$_2$O, trisodium citrate dihydrate, NaBH$_4$, HCl (conc.), tetraethoxysilane (TEOS), 3-aminopropyltrimethosilane (APS),

3-mercaptopropyltrimethoxysilane (MPS), H$_2$O$_2$ (28%), and sulfuric acid (98%) were supplied by Aldrich. Pluronic F127 (HO(CH$_2$CH$_2$O)$_{106}$(CH$_2$CH(CH$_3$)O)$_{70}$(CH$_2$CH$_2$O)$_{106}$OH), Brij58 ((CH$_2$CH$_2$O)$_{20}$C$_{16}$H$_{33}$), poly(diallyldimethylammonium chloride) (PDDA, average molecular weight = 100–200 kg mol^{-1}), poly(sodium 4-styrene-sulfonate) (PSS, average molecular weight = 70 kg mol^{-1}) and ascorbic acid (AA) were purchased from Sigma. Poly(vinylpyrrolidone) (PVP, average molecular weight = 10 kg mol^{-1}), cetyltrimethylammonium bromide (CTAB) and N,N-dimethylformamide (DMF) were supplied by Fluka. All chemicals were used as received. Pure grade ethanol and Milli-Q grade water were used as solvents.

Particle preparation

Gold nanodecahedra (44 nm side length) were prepared according to a previously reported procedure,[26] and were purified by several centrifugation (5000 rpm, 1 hour)–redispersion (in ethanol) cycles. Gold spheres (15 nm diameter) were synthesized by the Turkevich method[27] and used without further purification. Larger gold spheres (59 nm diameter) were synthesized according to a previously reported seed mediated method,[28] and purified by twofold centrifugation (4500 rpm, 30 min) and redispersion in water. Gold nanostars were synthesized and purified according to our previously published work.[29]

Glass preparation

Glass slides were cleaned with piranha solution (3 H$_2$SO$_4$: 1 H$_2$O$_2$) for 30 min, then copiously rinsed with pure water and kept under water until use. Dry glass slides were immersed either in a 0.01 M (in ethanol) solution of APS for 3 h (for 15 nm spheres and nanostars) or MPS for 1 h (for 59 nm spheres and decahedra), rinsed with ethanol and then immersed for a variable period of time in GNPs solution. Although most of the experiments presented in this paper were carried out using silanes to attach the particles, electrostatic interactions can also be used for binding, obtaining equivalent results. In this case, cleaned glass slides were immersed for 15 min in PDDA solution (positively charged polymer, 1 mg mL^{-1}, 0.5 M NaCl), rinsed with water, dried and then immersed in the spheres (d = 15 nm) solution for 2 min. For the adsorption of 59 nm spheres, a polymer layer with negative charge (PSS, 15 min, 1 mg mL^{-1} and 0.5 M NaCl solution) was added prior to GNP adsorption.

Preparation of mesoporous films

Silica mesoporous thin films were produced by spin-coating on top of the gold nanoparticle modified glass slides, at a spinning rate of 4000 rpm and using 125 μL of solution. The detailed sol preparation techniques were reported elsewhere.[30,31] Initial solutions comprised a TEOS : EtOH : template : H$_2$O : HCl mixture, with a 1 : 40 : 0.005 : 10 : 0.008 molar ratio when the template was F127, 1 : 40 : 0.05 : 10 : 0.008 for Brij58, and a 1 : 20 : 0.1 : 5 : 0.004 for CTAB. These solutions were aged for 72 h at room temperature prior to use. After spin-coating, the films were placed in 50% relative humidity chambers (obtained with a NaBr saturated solution) for 24 h and subjected to a stabilizing thermal treatment comprising two successive 24 h heat treatments at 60 °C and 120 °C, and a final 2 h step at

200 °C. The template was then removed by immersing the films in ethanol for 3 days. The final porosity (as determined by ellipsometry, see below) was 34% for Brij58 templated films and 39% for films templated with F127, indicating that the extraction treatment was successful.

Growth of covered nanoparticles

Au nanoparticles embedded in mesoporous silica films were grown by immersing the composite film in a solution containing $HAuCl_4$, CTAB and AA in different proportions. [$HAuCl_4$] was 6.25×10^{-5} M, the AA : Au molar ratio was varied between 2 and 32 and the CTAB : Au molar ratio was varied between 30 and 800.[32,33] The growth solution was replaced every 2 hours of reaction. After each growth step the films were copiously rinsed with water and dried in air before characterization.

Materials characterization

UV-visible-NIR spectra were recorded using an Agilent 8453 spectrophotometer. Transmission electron microscopy (TEM) analysis was performed with a JEOL JEM1010 microscope operating at an acceleration voltage of 100 kV. High resolution TEM (HRTEM) and scanning transmission electron microscopy (STEM) analyses were carried out in a JEOL JEM2010 FEG TEM operating at 200 kV. For HRTEM, lamellas were prepared by focused ion beam (FIB) lithography. Average mesopore size and film thickness were determined by environmental ellipsometric porosimetry (EEP SOPRA GES5A).[34] Film thickness and refractive index values were obtained from the ellipsometric parameters Ψ and Δ under different water relative pressures ($P/P°$, $P°$ being the saturation water vapor pressure at 25 °C), varying from 0 to 1. Water volume adsorbed at each $P/P°$ value was determined by modeling the obtained refractive index according to a three-component (water–air–oxide) effective medium approximation. Adsorption–desorption isotherms were then plotted using the water volume adsorbed by the porous film at each $P/P°$, and the mesoporous size was determined applying the Kelvin equation on these isotherms. In the present work, the equilibration time used at each $P/P°$ value was 40 s, while the measuring time was 10 s. Longer equilibration times (180 s) led to similar results.

Simulations of optical spectra were obtained using the boundary element method (BEM).[35] In the BEM, the electromagnetic fields are expressed in terms of surface integrals involving charge (σ_j) and current (h_j) distributions defined on the boundary of each region j. In our case, j runs over media representing gold (described by its measured frequency-dependent dielectric function taken from ref. 36), and air/porous silica mixture (air described by a constant refractive index—n—of 1 and porous silica described by $n = 1.33$, obtained from ellipsometry measurements). The particles were described by axially symmetric shapes capturing the main physical aspects of their response to external illumination. We have assimilated the particles to a central sphere of 30 nm radius with either one or two (located at opposite sides of the sphere) spherically capped rod-shaped tips of length L and diameter D. Convergence was achieved with 250 parameterization points.

Results and discussion

We focused this work on the seeded growth of GNPs embedded within mesoporous thin silica films. The effects of the film pore size and the growth reaction parameters were studied so as to identify the key parameters that determine the GNPs final shape and optical properties. The first synthesis step comprised the attachment of the seed GNPs onto a glass surface (by either chemical bonding or electrostatic interactions), followed by coverage with templated sol–gel silica thin films. The coverage step was carried out by spin coating and post-treatment of the obtained thin films, as typically carried out on pure glass substrates. This approach was previously demonstrated for decahedra,[25] but we applied it here to nanoparticles with different sizes and shapes (spheres and nanostars besides decahedra), as well as thin films with different pore sizes. The full list of synthesized materials is presented in Table 1 and representative TEM images of some of the obtained composite materials are shown in Fig. 1.

In all samples, uniform films were obtained fully covering the nanoparticles and presenting well-ordered mesoporous channels. According to the TEM images, the pores of SF and SB films seem to be ordered in an $Im3m$ cubic phase with [110] planes oriented parallel to the substrate, which is the commonly obtained phase when using F127 or Brij58 as templates.[37] This demonstrates that the formation of the mesoporous thin films was not affected by the (nanoscale) roughness of the substrate, in good agreement with previous results that show that the pore symmetry of a mesoporous overlayer is only affected when thicker obstacles

Table 1 Description of the synthesized samples. Interpore distances were obtained from TEM images, d = diameter; l = edge length

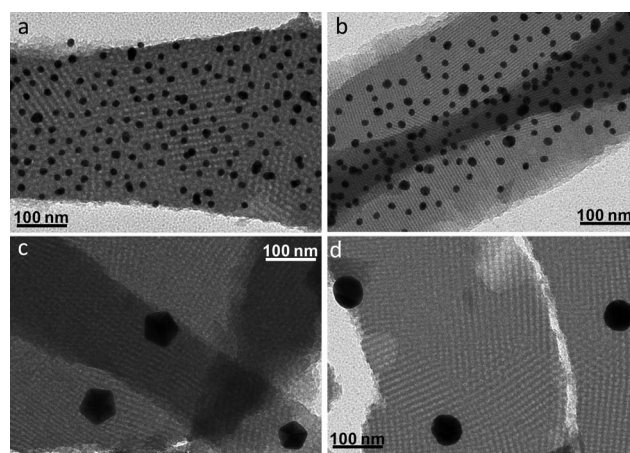| Particle type	Particle size/nm	Mesoporous film	Interpore distance/nm	Sample name
Spheres	$d = 15$	SiO_2–F127	13 ± 1	S_{15}@SF
		SiO_2–Brij58	4.7 ± 0.5	S_{15}@SB
	$d = 59$	SiO_2–F127	13 ± 1	S_{60}@SF
Decahedra	$l = 44$	SiO_2–F127	13 ± 1	D@SF
Stars		SiO_2–CTAB	4.7 ± 0.5	St@SC

Fig. 1 Representative TEM images of samples S_{15}@SF (a), S_{15}@SB (b), D@SF (c) and S_{60}@SF (d). See Table 1 for sample definitions.

(in the order of hundreds of nm) act as anchoring points for topological defects.[38] Regarding the particles, XPS experiments have demonstrated that they are not in contact with air and remain around their original positions in the glass/film interface.[25] HRTEM images from specimens prepared in cross-section confirm this result (see below). In the TEM images (Fig. 1) the particles appear uniformly dispersed within the film, with no significant aggregation, and the shapes of Au nanospheres and decahedra seem to remain unaltered after the thermal treatment. Besides, UV-visible-NIR spectroscopy (Fig. S1, ESI†) shows that the optical properties of these particles were almost unaltered by film deposition and treatment, confirming that no aggregation or reshaping occurred during film processing. It should be pointed out that, in the case of decahedra and 59 nm spheres, although the shape of the LSPR was maintained, the band maximum position was red-shifted because of the increase in local n, which varied from $n = 1$ (air) up to ~1.2 to 1.3 (porous SiO_2).[29] For 15 nm spheres this shift was not noticeable, because of their lower sensitivity to refractive index changes.[39]

Interestingly, for Au nanostars (sample St@SC), deformation of the particles during processing was observed in both the UV-visible-NIR spectra and TEM images, showing that nanostars convert into "faceted spheres" (see Fig. S2, ESI†). Such deformation arises from the intrinsic instability of crystallographically defective nanostar tips[40] toward thermal heating, when submitted to the temperatures required to stiffen the silica network (up to 200 °C). Thus, encapsulation of nanoparticles with tips (which are particularly appealing for sensing applications) within mesoporous films is not feasible by means of this method. Therefore, we decided to attempt the *in situ* growth of branches from encapsulated nanoparticles, making use of the pores in the film as templates. It has been previously shown that encapsulated particles (within either porous polymers or mesoporous silica) can be homogeneously or heterogeneously grown,[23,32,33] by simple addition of a solution containing a gold salt, a surfactant (CTAB) and a mild reducing agent (ascorbic acid, AA). AA easily reduces Au(III) to Au(I), which remains stable in solution by complexation onto CTAB micelles.[41] Subsequent reduction from Au(I) to Au^0 takes place selectively onto the Au seeds, which act as catalysts.

Effect of pore size

To understand the effect of the size of mesopores on the growth of GNPs, we used 15 nm spheres covered with both SiO_2–F127 and SiO_2–Brij58 thin films (S_{15}@SF and S_{15}@SB samples, respectively). The pore array was found to be body centered cubic (*Im3m*) in both cases and the measured film thickness was also similar, the pore diameter and wall thickness (*i.e.* the interpore distance) being the main difference between both film types (Table 1). A solution with a molar ratio of CTAB : AA : Au = 60 : 16 : 1 was used for the growth. The evolution of the UV-visible-NIR spectra as a function of reaction time as well as representative TEM images of the final samples (after 6 h of reaction) are shown in Fig. 2.

For S_{15}@SF samples, at short reaction times, no significant spectral changes are observed, while after 4 h of reaction, a second band appears at a longer wavelength (*ca.* 620 nm, Fig. 2a), which remains with increased intensity at 6 h of reaction time. These spectra closely resemble those previously reported for Au nanostars,[29] with a lower wavelength band attributed to a dipolar LSPR localized in the central core and another at a higher wavelength from the dipolar plasmon modes localized at the tips. In this framework, an increase in the intensity of the long wavelength band would be attributed to an increase in the number of tips present in the sample as well as in the tip's length.[29] In this case, as the seed particles have a size that is similar to the interpore distance and thus are in contact with
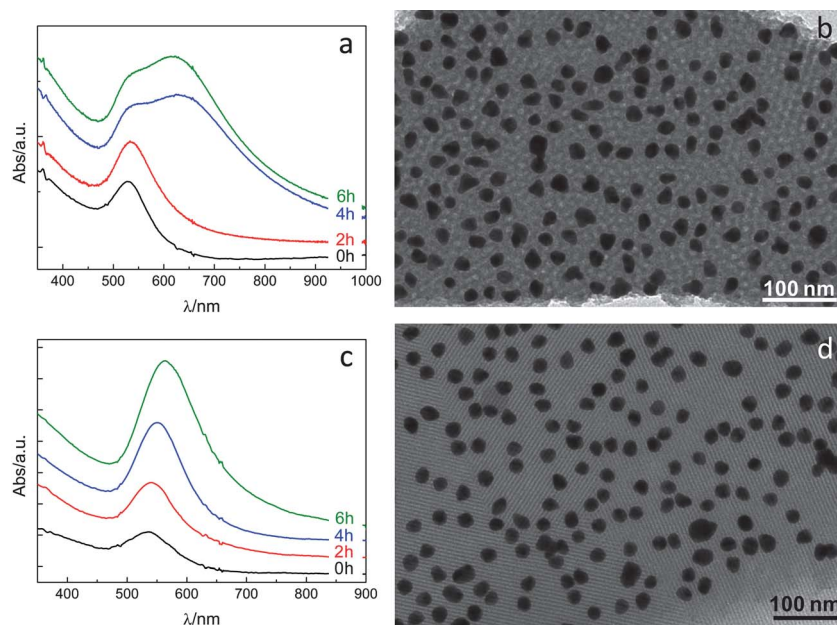

Fig. 2 Left: UV-visible-NIR spectra as a function of reaction time for S_{15}@SF (a) and S_{15}@SB (c) samples grown with CTAB : AA : Au solution with 60 : 16 : 1 molar ratio; the spectra were shifted upward to improve visibility. Right: TEM images of the same samples after 6 h of reaction (b and d for S_{15}@SF and S_{15}@SB, respectively).

Table 2 Evolution of average particle size at different reaction times for $S_{15}@SF$ and $S_{15}@SB$ samples grown with a solution of CTAB, AA and Au with 60 : 16 : 1 molar ratio. The data were obtained by analyzing several TEM images

Sample	Reaction time/h	Short axis length/nm	Long axis length/nm	"AR"
$S_{15}@SF$	0	13 ± 1	15 ± 2	1.1 ± 0.1
	2	15 ± 2	20 ± 4	1.3 ± 0.3
	4	17 ± 2	23 ± 5	1.3 ± 0.2
	6	17 ± 2	25 ± 5	1.5 ± 0.3
$S_{15}@SB$	0	14 ± 2	16 ± 3	1.1 ± 0.1
	6	22 ± 2	24 ± 2	1.1 ± 0.1

a limited amount of pores, most of them present only one or two tips. However, from the TEM images one can see that an increased number of particles develop tips as the reaction proceeds (Fig. 2b). For the $S_{15}@SB$ samples, a gradual shift of the main band in the UV-visible-NIR spectrum is observed (from 536 to 562 nm), along with an increase in intensity (Fig. 2c). This variation can be attributed to an increase in particle size without significant morphological changes, which was confirmed by TEM analysis (Fig. 2d and Table 2).

An "average aspect ratio" ("AR") of the particles can be estimated by measuring (in TEM images) the longer and the shorter axes of each particle and averaging the results. This "AR" and the dimensions of the long and short axes, as a function of reaction time, are listed in Table 2. Thus, the main conclusion from this analysis is that for $S_{15}@SB$ samples the "AR" of the particles remains constant, in contrast with $S_{15}@SF$ samples, in which a gradual increase in the "AR" is observed. The variation of total particle size (from 14 to 22 nm in the short axis and from 16 to 24 nm in the longer axis) without change in the "AR" observed in $S_{15}@SB$ samples points toward some local dissolution or reordering of the silica matrix, allowing the quasi-isotropic growth of the GNPs. Variation in the mesoporosity of

the thin films after the growth treatment was evaluated by environmental ellipsometric porosimetry (EEP).[42] Due to the difficulty of modeling samples with spectral variation along with changes in the refractive index (as is the case of our samples due to the presence of plasmonic particles), the measurements were carried out on samples prepared without GNPs. The samples were treated with the growth solution under the same conditions used for the GNP containing films. Fig. 3 shows the water adsorption–desorption isotherms, obtained by EEP, for the films before and after treatment with the growth solution. The values for pore and neck sizes and total pore volume (porosity) obtained from these measurements are presented in Table 3, together with the film thicknesses obtained by ellipsometry and contact angle values. In both cases, the isotherms before and after the treatment are remarkably similar to each other, indicating that the pore size and arrangement have not been significantly affected. For the SF sample, a slight shift of the adsorption branches towards higher $P/P°$ values suggests that treated samples present slightly larger pores. Analysis using the Kelvin equation, and taking into account the hydrophilicity of the sample (*i.e.*, contact angle, see Table 3), shows that pore and neck sizes are somewhat increased after the treatment in both samples, suggesting that some dissolution could take place though not extensively, as the isotherms still show the typical Type IV shape with H1 hysteresis loop expected for caged mesoporous materials. Surprisingly, neck diameters for SF and SB samples are quite similar. This small interpore connection in the larger pore samples (SF) can be attributed to a combination of two factors: (a) the F127 : Si ratio of 0.005 leads to a *Im3m* pore system derived from micelle packing with relatively narrow pore entrances,[43] and (b) the mild treatment applied (200 °C followed by extraction) is not enough to coarsen the pore entrances.[44]

We also observed that the thickness of the treated films is slightly smaller (~10%) than that of untreated films. Although surface dissolution of the film cannot be ruled out, it is very
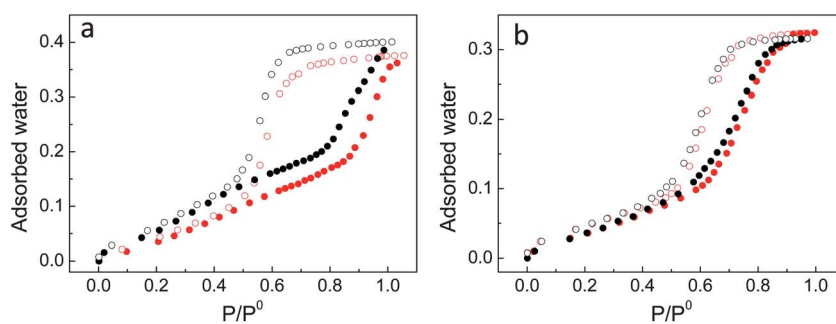

Fig. 3 Adsorption/desorption isotherms of SF (a) and SB (b) films determined through EEP, before (black) and after (red) treatment with growth solution. Adsorption data are shown in full circles and desorption data in open circles.

Table 3 Pore and neck sizes obtained by EEP and thickness values determined by ellipsometry

Sample	Porosity (%)	Neck diameter/nm	Pore diameter/nm	Contact angle/°	Film thickness/nm
SF	39	1.5 ± 0.2	7.5 ± 1.5	80 ± 2	107
SF + 6 h in growth solution	37	1.8 ± 0.2	8.8 ± 1.5	73 ± 1	95
SB	34	1.5 ± 0.2	2.4 ± 0.5	82 ± 2	83
SB + 6 h in growth solution	35	1.8 ± 0.3	2.9 ± 0.6	72 ± 4	75

unlikely to happen,[42] so this difference in thickness is probably a consequence of film contraction due to the enhanced condensation of the framework after acidic treatment (solution pH around 4, due to the presence of AA). Thus, EEP analysis demonstrated that an extra condensation due to the acid treatment, accompanied by a small degree of dissolution, may occur and be responsible for the observed pore and interpore neck widening. However, the mesoporous structure is preserved upon immersion in the growth solution. Local dissolution around the GNPs cannot be ruled out, and we expect it to be favored in the case of SB films, as Brij58 templated oxides typically have thinner walls than F127 templated ones.[37]

Finally, STEM, elemental mapping and HRTEM measurements were performed on the S_{15}@SF sample after growth for 6 h; selected images are presented in Fig. 4. The cross-section and elemental analysis results confirm that the particles are fixed at the glass/film interface and no Au nucleation is observed in other regions of the film. Unfortunately, direct information on the insertion of the tips in the mesopore structure could not be obtained with these measurements, as the pores could not be imaged, possibly due to damage generated by the FIB treatment. Both mono- and polycrystalline tips were found in the sample, but the sizes were always similar to the interpore distance of the oxide. In some cases, the size measured for the tips was larger than the pore size, most likely due to local dissolution of the oxide. However, it is important to note that this dissolution is not generalized, as the EEP measurements have demonstrated. After this first set of experiments, which confirms that 15 nm diameter spherical GNPs covered with SiO_2–F127 thin films can be grown using the pores as templates, a thorough study of the influence of reagent concentrations (CTAB and AA) on the final shape and optical properties of the particles was carried out, as described below.
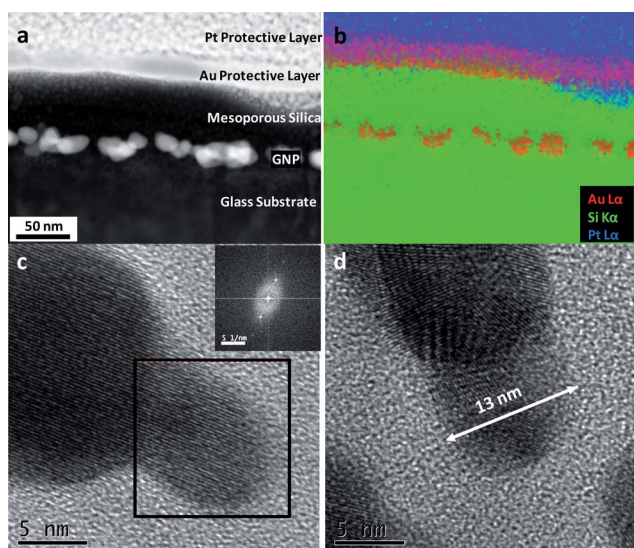

Fig. 4 (a) STEM dark field image of a cross-section lamella prepared by FIB, showing the GNP arrangement inside the SF film. (b) STEM-XEDS mapping of the section displayed in (a); during the lamella preparation the surface of the sample was protected with a sputtered Au layer; (c) HRTEM image of one tip showing the Au lattice image and the Fourier transform of the framed area, confirming the single-crystalline structure of the tip; the spots have a d_{hkl} of 2.33 Å, assigned to (111) Au reflections. (d) Example of a polycrystalline tip, characteristic of thicker particles.

Effect of [CTAB] and [AA]

CTAB concentration has been reported to be a determining factor on the seeded growth of pNIPAM encapsulated GNPs,[32,33] mainly due to changes in the growth kinetics. Therefore, we studied the growth of S_{15}@SF at different CTAB : Au molar ratios, ranging from 30 to 800. The growth of 15 nm Au spheres was monitored as a function of time ($[Au^{3+}] = 6.25 \times 10^{-5}$ M, AA : Au = 16) by means of UV-visible-NIR spectroscopy and TEM, and the results are summarized in Fig. 5 and Table 4. The variation of [CTAB] was indeed found to significantly affect the resulting particle morphology, since a decrease in [CTAB] leads to NPs with more numerous and longer tips
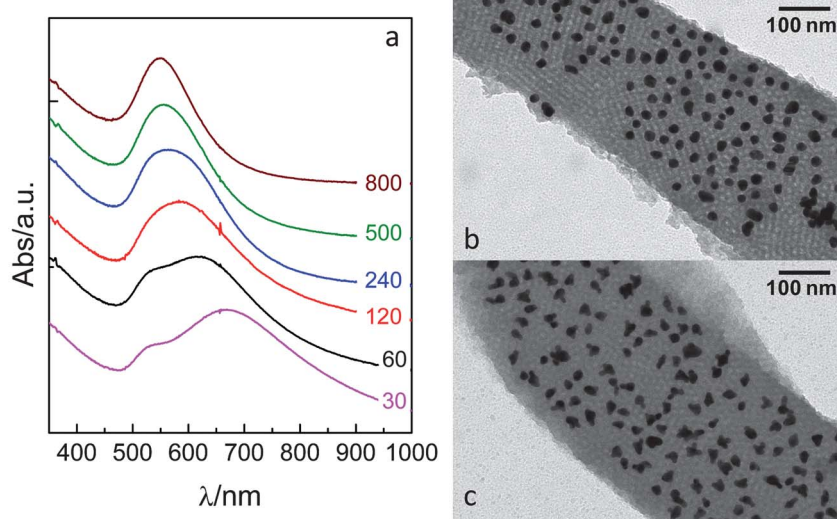

Fig. 5 Effect of [CTAB] on the growth of S_{15}@SF with AA : Au = 16. (a) UV-visible-NIR spectra as a function of CTAB : Au molar ratio (as indicated in the labels) after 6 h of reaction; the spectra were shifted upward to improve visibility. Representative TEM images of the highest (b) and the lowest (c) [CTAB].

Table 4 Average particle size after 6 h of growth under different conditions, as indicated, for the S$_{15}$@SF sample. The data were obtained by analyzing several TEM images

CTAB : Au	AA : Au	Short axis length/nm	Long axis length/nm	"AR"
30	16	16 ± 2	27 ± 6	1.7 ± 0.3
60		17 ± 2	25 ± 5	1.5 ± 0.3
120		19 ± 2	25 ± 4	1.4 ± 0.2
240		18 ± 2	24 ± 3	1.4 ± 0.2
500		17 ± 2	21 ± 3	1.2 ± 0.1
800		17 ± 2	21 ± 3	1.2 ± 0.1
60	2	20 ± 2	26 ± 3	1.3 ± 0.2
	8	21 ± 3	28 ± 5	1.3 ± 0.2
	32	19 ± 2	27 ± 3	1.4 ± 0.2

(Fig. 5b and c), which is also reflected in spectral changes as discussed above (Fig. 5a and S3, ESI†). Apart from the kinetic effects derived from CTAB concentration, steric hindrance may also play a role, since the gold ions are complexed to CTAB micelles, which must diffuse through the pores and necks of the mesoporous material. When the CTAB concentration is lower, fewer micelles are formed and lower steric hindrance is expected. Finally, it is important to note that in the absence of CTAB, nucleation of spherical GNPs was immediately observed in the growth solution (outside the silica thin film).

The effect of varying [AA] is less important than for CTAB, as can be seen in Table 4 (and Fig. S4, ESI†). The more anisotropic particles were obtained for molar ratios higher than 16 (AA > 16), for lower AA concentrations (ratios 2 and 8), the obtained particles were more isotropic (i.e., lower "AR", Table 4 and Fig. S4, ESI†). These differences can also be attributed to

changes in the reaction rate, being higher when the concentration of reducing agent is higher and thus giving rise to more anisotropic particles.

Generalization and optical modeling

We have demonstrated so far the templated seeded growth of branches from citrate-capped 15 nm Au spheres covered with SiO$_2$–F127 mesoporous thin films. Given the variety of existing synthetic methods, comprising different morphologies and surface chemistry, it is important to demonstrate the general validity of the process. To this end, SF mesoporous thin films were used as templates to grow larger nanoparticles, both spheres (59 nm diameter, CTAB capping) and decahedra (44 nm side length, PVP capping). Interestingly, despite the different crystallographic facets and surface chemistry, in both cases we observed the growth of multiple branches, along with the corresponding spectral changes, as shown in Fig. 6. Because of the larger core sizes, it can be clearly appreciated that the branches grow, through the pores, from various sites at the NPs surface. The increased number of growth sites per particle also leads to an apparently faster reaction rate, as compared with the 15 nm spheres, since changes in the spectra are visible after just 1 hour of reaction for the 59 nm spheres or even 30 min for decahedra. Analysis of the TEM images reveals that the core size remains constant whereas the branches display dimensions related to the pore size (see an example in Table S1, ESI†). For the sample S$_{60}$@SF after 6 h of reaction, STEM and HRTEM pictures (Fig. S5, ESI†) confirm that tips can be poly- or mono-crystalline, mainly depending on tip size, and that some tips are bigger than the pore size, as shown for S$_{15}$@SF samples. In the case of decahedra, although at first sight it may
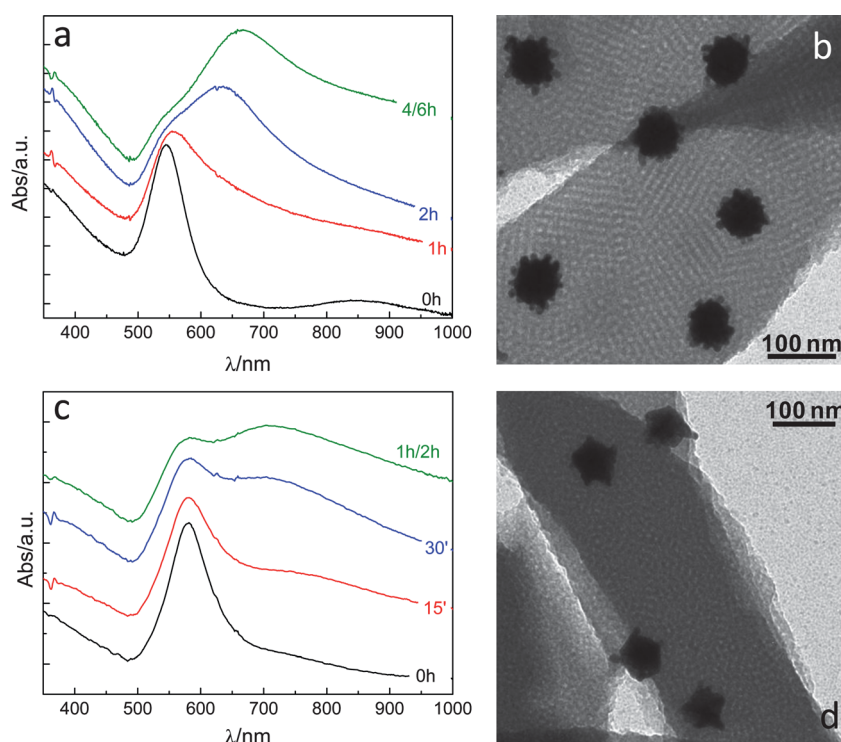

Fig. 6 UV-visible-NIR spectra of S$_{60}$@SF (a) and D@SF (c) grown with CTAB : AA : Au solution with 60 : 16 : 1 molar ratio, as a function of reaction time; the spectra were shifted upward to improve visibility. TEM images of the same samples after 6 h (b) and 2 h (d) of reaction.
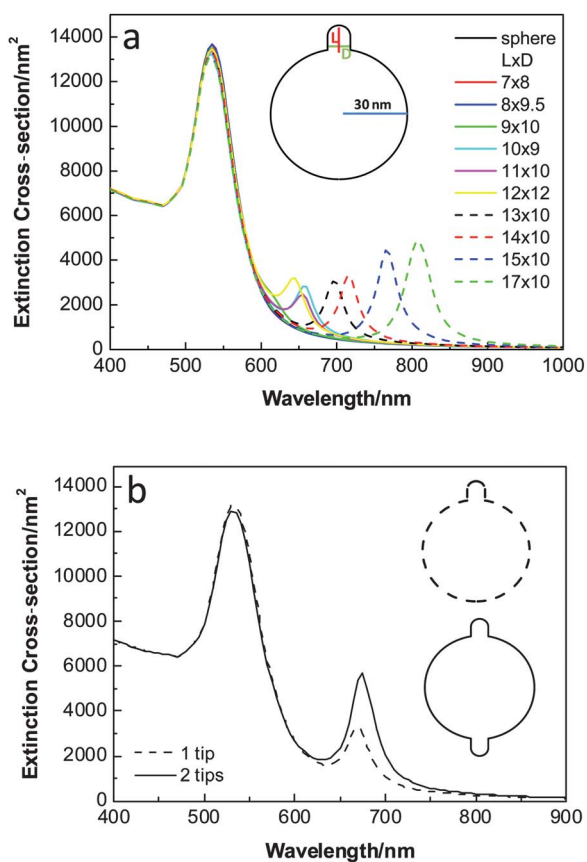
Fig. 7 BEM extinction spectra for particles containing tips with: (a) different diameters (*D*) and lengths (*L*), as labeled, and (b) with either 1 or 2 tips. The morphologies corresponding to the calculations are depicted as insets.

seem that the branches grow preferentially from the apexes, careful analysis of several TEM images shows that they grow at random sites around the particles.

These results demonstrate that the growth is not affected by the morphology or surface chemistry of the particles used as seeds, which opens up opportunities for synthesizing metal nanoparticles of very diverse shapes. This is especially interesting as the tips can only grow in the direction of the pores and not in the direction of the substrate, resulting in Janus-like nanoparticles with a non-uniform distribution of tips, not easily obtainable by traditional colloid chemistry methods. An example of this type of particles is shown in Fig. S6 (ESI†) and further work is underway to fully characterize these novel nanoparticles.

Since these samples show better defined morphologies, they can be used for modeling the optical properties. On the basis of the TEM analysis (Table S1† and histograms of branch size distribution, not shown) we carried out numerical calculations of the UV-visible-NIR spectra, for dimensions corresponding to the S$_{60}$@SF sample grown for 6 h (Fig. 7). The calculations were based on the boundary element method (BEM),[35] which can be readily applied to objects with arbitrary shapes and axial symmetry. For the present case, a geometrical model comprising a central sphere with either one or two spherically capped rod tips was employed, as depicted in the insets of Fig. 7. Two bands are indeed obtained, corresponding to core and tip plasmon

modes, in agreement with the experimental spectra. We depicted in Fig. 7a the spectra resulting from variations in the branch dimensions, which show that the position of the LSPR tip mode is strongly dependent on both tip length and width. As the actual particles present a wide variety of branches with different sizes, the average experimental spectrum would be the result of adding the response from each tip, giving rise to a broad extinction band. The intensity ratio between both bands in the experimental spectra can be explained taking into account the results presented in Fig. 7b. Indeed, the relative intensity of the LSPR tip band is observed to increase when an additional tip is included, so the large number of tips on each particle would result in the predominance of the higher wavelength band.

Conclusions

We have demonstrated that it is possible to obtain composite materials containing a submonolayer of GNPs with arbitrary shapes covered with mesoporous silica thin films. We have also demonstrated that the shape of the particles, and thus their optical properties, can be modified by standard seeded growth. By adjusting the CTAB and ascorbic acid concentrations, the anisotropy of the grown nanoparticles can be varied, so that they can branch through the pores of the mesoporous silica film, which is also influenced by pore size. When the interpore distance is increased from 6 up to 12 nm, the final morphology varies from isotropic to anisotropic or branched structures. The obtained composite materials combine the interesting optical properties of metal nanoparticles (which can be tuned through the reaction conditions), the filtering ability of mesoporous thin films and the chemical reactivity of silica. All these properties combined in one single composite material opens up the possibility of applications in several fields, including catalysis, (bio)sensing and non-linear optics.

References

1 M.-C. Daniel and D. Astruc, *Chem. Rev.*, 2003, **104**, 293–346.
2 R. A. Sperling, P. Rivera Gil, F. Zhang, M. Zanella and W. J. Parak, *Chem. Soc. Rev.*, 2008, **37**, 1896–1908.
3 C. F. Bohren and D. R. Huffman, *Absorption and Scattering of Light by Small Particles*, Wiley-Interscience, New York, 1983.
4 U. Kreibig and M. Vollmer, *Optical Properties of Metal Clusters*, Springer, 1995.
5 A. Moores and F. Goettmann, *New J. Chem.*, 2006, **30**, 1121–1132.
6 L. M. Liz-Marzan, *Langmuir*, 2006, **22**, 32–41.
7 Y. Xia, Y. Xiong, B. Lim and S. E. Skrabalak, *Angew. Chem., Int. Ed.*, 2009, **48**, 60–103.
8 M. Grzelczak, J. Pérez Juste, P. Mulvaney and L. M. Liz Marzán, *Chem. Soc. Rev.*, 2008, **37**, 1783–1791.
9 R. Alvarez-Puebla, L. M. Liz-Marzán and F. J. García de Abajo, *J. Phys. Chem. Lett.*, 2010, **1**, 2428–2434.
10 C. Sanchez, C. Boissière, D. Grosso, C. Laberty and L. Nicole, *Chem. Mater.*, 2008, **20**, 682–737.

11 G. J. A. A. Soler-Illia, C. Sanchez, B. Lebeau and J. Patarin, *Chem. Rev.*, 2002, **102**, 4093–4138.

12 Special Issue on Templated Materials, ed. M. Jaroniec and F. Schüth, *Chem. Mater.*, 2008, **20**, 599–1190, and references therein.

13 J. Sun and X. Bao, *Chem.–Eur. J.*, 2008, **14**, 7478–7488.

14 G. Walters and I. P. Parkin, *J. Mater. Chem.*, 2009, **19**, 574–590.

15 R. J. White, R. Luque, V. L. Budarin, J. H. Clark and D. J. Macquarrie, *Chem. Soc. Rev.*, 2009, **38**, 481–494.

16 M. D. Pérez, E. Otal, S. A. Bilmes, G. J. A. A. Soler-Illia, E. L. Crepaldi, D. Grosso and C. Sanchez, *Langmuir*, 2004, **20**, 6879–6886.

17 M. C. Fuertes, M. Marchena, M. C. Marchi, A. Wolosiuk and G. J. A. A. Soler-Illia, *Small*, 2009, **5**, 272–280.

18 E. D. Martínez, M. G. Bellino and G. J. A. A. Soler-Illia, *ACS Appl. Mater. Interfaces*, 2009, **1**, 746–749.

19 T.-C. Wei and H. W. Hillhouse, *Langmuir*, 2007, **23**, 5689–5699.

20 M. Etienne, A. Quach, D. Grosso, L. Nicole, C. Sanchez and A. Walcarius, *Chem. Mater.*, 2007, **19**, 844–856.

21 H.-Y. Lian, Y.-H. Liang, Y. Yamauchi and K. C. W. Wu, *J. Phys. Chem. C*, 2011, **115**, 6581–6590.

22 M. A. Carreon, S. Y. Choi, M. Mamak, N. Chopra and G. A. Ozin, *J. Mater. Chem.*, 2007, **17**, 82–89.

23 Z. Li, C. Kübel, V. I. Pârvulescu and R. Richards, *ACS Nano*, 2008, **2**, 1205–1212.

24 L. Bois, F. Chassagneux, C. Desroches, Y. Battie, N. Destouches, N. Gilon, S. Parola and O. Stéphan, *Langmuir*, 2010, **26**, 8729–8736.

25 P. C. Angelomé and L. M. Liz-Marzán, *J. Phys. Chem. C*, 2010, **114**, 18379–18383.

26 A. Sánchez-Iglesias, I. Pastoriza-Santos, J. Pérez Juste, B. Rodríguez-González, F. J. García de Abajo and L. M. Liz Marzán, *Adv. Mater.*, 2006, **18**, 2529–2534.

27 J. Turkevich, P. C. Stevenson and J. Hillier, *Discuss. Faraday Soc.*, 1951, **11**, 55–75.

28 J. Rodríguez-Fernández, J. Pérez-Juste, F. J. García de Abajo and L. M. Liz-Marzán, *Langmuir*, 2006, **22**, 7007–7010.

29 P. Senthil Kumar, I. Pastoriza-Santos, B. Rodríguez-González, F. J. García de Abajo and L. M. Liz-Marzán, *Nanotechnology*, 2008, **19**, 015606.

30 D. Grosso, A. R. Balkenende, P. A. Albouy, A. Ayral, H. Amenitsch and F. Babonneau, *Chem. Mater.*, 2001, **13**, 1848–1856.

31 D. Grosso, A. R. Balkenende, P. A. Albouy, M. Lavergne, L. Mazerolles and F. Babonneau, *J. Mater. Chem.*, 2000, **10**, 2085–2089.

32 R. Contreras-Cáceres, A. Sánchez-Iglesias, M. Karg, I. Pastoriza-Santos, J. Pérez-Juste, J. Pacifico, T. Hellweg, A. Fernández-Barbero and L. M. Liz-Marzán, *Adv. Mater.*, 2008, **20**, 1666–1670.

33 R. Contreras-Cáceres, J. Pacifico, I. Pastoriza-Santos, J. Pérez Juste, A. Fernández-Barbero and L. M. Liz-Marzán, *Adv. Funct. Mater.*, 2009, **19**, 3070–3076.

34 C. Boissiere, D. Grosso, S. Lepoutre, L. Nicole, A. B. Bruneau and C. Sanchez, *Langmuir*, 2005, **21**, 12362–12371.

35 F. J. García de Abajo and A. Howie, *Phys. Rev. B: Condens. Matter Mater. Phys.*, 2002, **65**, 115418.

36 P. B. Johnson and R. W. Christy, *Phys. Rev. B: Solid State*, 1972, **6**, 4370.

37 E. L. Crepaldi, G. J. A. A. Soler-Illia, D. Grosso, F. Cagnol, F. Ribot and C. Sanchez, *J. Am. Chem. Soc.*, 2003, **125**, 9770–9786.

38 A. Zelcer, A. Wolosiuk and G. J. A. A. Soler-Illia, *J. Mater. Chem.*, 2009, **19**, 4191–4196.

39 A. Bourgeois, A. Brunet Bruneau, S. Fisson, B. Demarets, D. Grosso, F. Cagnol, C. Sanchez and J. Rivory, *Thin Solid Films*, 2004, **447–448**, 46–50.

40 L. Rodriguez-Lorenzo, J. M. Romo-Herrera, J. Perez-Juste, R. A. Alvarez-Puebla and L. M. Liz-Marzan, *J. Mater. Chem.*, 2011, **21**, 11544–11549.

41 J. Pérez-Juste, L. M. Liz-Marzán, S. Carnie, D. Y. C. Chan and P. Mulvaney, *Adv. Funct. Mater.*, 2004, **14**, 571–579.

42 J. D. Bass, D. Grosso, C. Boissiere, E. Belamie, T. Coradin and C. Sanchez, *Chem. Mater.*, 2007, **19**, 4349–4356.

43 T.-W. Kim, R. Ryoo, M. Kruk, K. P. Gierszal, M. Jaroniec, S. Kamiya and O. Terasaki, *J. Phys. Chem. B*, 2004, **108**, 11480–11489.

44 Y. Sakatani, D. Grosso, L. Nicole, C. Boissiere, G. J. A. A. Soler-Illia and C. Sanchez, *J. Mater. Chem.*, 2006, **16**, 77–82.